NANO LETTERS

2007
Vol. 7, No. 2
439−445

Electrostatic Funneling for Precise Nanoparticle Placement: A Route to Wafer-Scale Integration

Liang-Chieh Ma, Ramkumar Subramanian, Hong-Wen Huang, Vishva Ray, Choong-Un Kim, and Seong Jin Koh*

Department of Materials Science and Engineering, The University of Texas at Arlington, Arlington, Texas 76019

Received November 21, 2006

ABSTRACT

We demonstrate a large-scale placement of nanoparticles through a scheme named "electrostatic funneling", in which charged nanoparticles are guided by an electrostatic potential energy gradient and placed on targeted locations with nanoscale precision. The guiding electrostatic structures are defined using current CMOS fabrication technology. The effectiveness of this scheme is demonstrated for a variety of geometries including one-dimensional and zero-dimensional patterns as well as three-dimensional step structures. Placement precision of 6 nm has been demonstrated using a one-dimensional guiding structure comprising alternatively charged lines with line width of ~100 nm. Detailed calculations using DLVO theory agree well with the observed long-range interactions and also estimate lateral forces as strong as (1–3) $\times 10^{-7}$ dyn, which well explains the observed guided placement of Au nanoparticles.

Recently, a lot of attention has been given to fabricating electronic/optical devices and biological/chemical sensors made of nanoscale building blocks such as nanoparticles,[1−3] nanowires,[4−9] carbon nanotubes,[10−12] DNA,[13,14] and proteins.[13,15,16] For the practical realization of such devices/sensors, one of the key requirements is the ability to simultaneously place the individual building blocks on exact substrate locations over a large area. Many approaches have been explored, including microfluids,[17,18] electric fields,[19,20] magnetic field,[21] surface functionalization,[22−26] surface steps,[9] capillary forces,[27−29] biological templates,[30−35] and scanning probe microscopy.[22,36] Although these approaches have had significant success, at this time techniques that appear suitable for wafer-scale implementation are few. In this Letter, we demonstrate large-scale placement of nanoparticles using an "electrostatic funnel" that guides charged nanoparticles onto targeted locations predefined on the substrate. The simplicity of the guided placement in addition to its compatibility with current CMOS fabrication technology may provide a practical means of fabricating integrated systems of nanoscale devices.

The electrostatic funneling concept is illustrated by an example in Figure 1, where a substrate having a surface pattern of alternating lines is functionalized with positively and negatively charged molecules. When the substrate is immersed into a colloidal solution containing charged nanoparticles, the substrate and nanoparticles interact in the liquid medium via electrical double-layer interaction.[37−39]

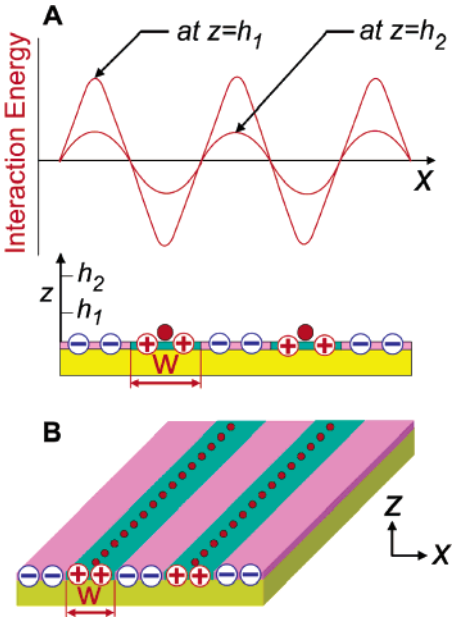

Figure 1. Wafer-scale nanoparticle placement with electrostatic funneling. (A) A schematic of the electrostatic interaction energy in an aqueous solution for a negatively charged nanoparticle near a substrate surface functionalized with positively and negatively charged molecules. (B) The nanoparticles (red dots) are guided to the centers of positively charged lines (of width *W*) where the interaction energy is minimum.

Simple electrostatic consideration shows that, near the substrate surface, the interaction energy between a negatively charged nanoparticle and the substrate has minima and maxima as displayed in Figure 1. When the charged

* Corresponding author: tel, 817-272-1223; fax, 817-272-2538; e-mail, skoh@uta.edu.

10.1021/nl062727c CCC: $37.00
Published on Web 01/05/2007

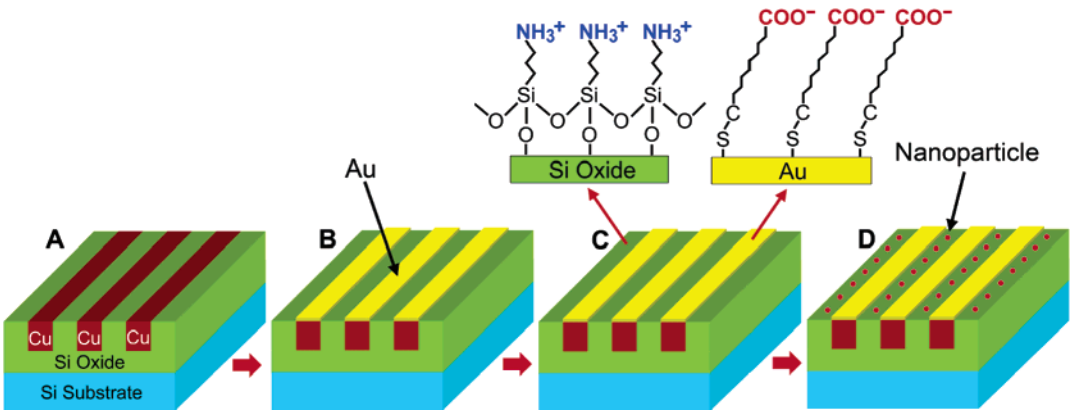

Figure 2. Experimental procedure. (A) Starting structure in which copper interconnect lines (brown) are embedded in the silicon oxide dielectric (green) fabricated on a 200 mm silicon wafer. (B) Exposed copper lines are electroless plated with gold. (C) Selective formation of self-assembled monolayers (SAMs). SAMs of APTES ($-NH_2$; $-NH_3^+$) are selectively formed on silicon oxide surfaces and SAMs of MHA ($-COOH$; $-COO^-$) are selectively formed on gold surfaces, providing positively and negatively charged lines, respectively, in an aqueous solution. (D) Immersion into colloidal solution containing negatively charged Au nanoparticles.

nanoparticle is being attracted to a positively charged line, the *gradient* of the interaction energy in a direction parallel to the substrate (*x* direction in Figure 1) produces *lateral* forces that push it toward the center of the positively charged line, a low-energy site. Because an entire wafer could be functionalized at the same time, this guiding mechanism may be able to allow concurrent large-scale nanoparticle placement over an entire wafer. As will be shown later in this paper, when the interaction energy gradient is sufficiently strong, nanoparticles can be placed along a line with nanometer scale precision even though the guiding structures are defined in much larger scale, on the order of ~100 nm.

Figure 2 outlines the experimental procedures used to demonstrate the concept of electrostatic funneling. We started the experiment with a common interconnect structure of alternating lines of copper and silicon oxide fabricated with damascene technology[40] on a 200 mm silicon wafer, Figure 2A. It should be noted that, being planarized by chemical-mechanical polishing (CMP),[40] the surface of the copper and silicon oxide lines were almost flat (roughness: 1−2 nm) and had negligible height difference, with the copper lines being lower than silicon oxide lines by ~5 nm as measured with an atomic force microscope (AFM, Digital Instruments Dimension 5000). The line widths were 120 and 80 nm for copper and silicon oxide, respectively. The wafer was cut (typically, 2 cm × 2 cm), cleaned with acetone, and then UV ozone cleaned (PSD-UVT, NovaScan) for 30 min. The wafer was then immersed into 1% citric acid solution (Sigma-Aldrich) for 15 min to remove any copper oxide on the surface of copper lines and rinsed with deionized water. We then selectively coated the copper lines with a thin layer of gold (thickness ~15 nm) using electroless plating,[41] producing alternating lines of gold and silicon oxide, Figure 2B, and making the Au-coated copper lines ~10 nm higher than silicon oxide lines, as measured with the AFM. Positively and negatively charged self-assembled monolayers (SAMs) were formed on lines of silicon oxide and gold using (3-aminopropyl)triethoxysilane (APTES, $(C_2H_5O)_3-Si-(CH_2)_3-NH_2$, 99%; Sigma-Aldrich) and 16-mercaptohexadecanoic acid (MHA, $HS-(CH_2)_{15}-COOH$, 99%; ProChimia, Poland), respectively.[42,43] The APTES SAMs were formed by immersing the wafer into 1 mM of APTES in chloroform for 30 min at room temperature, followed by rinsing with 2-propanol and drying with nitrogen. The MHA SAMs were formed using 5 mM MHA solution in ethanol for 3 h at room temperature, followed by rinsing in a 1% solution of HCl in ethanol for 15 s and then with absolute ethanol (200 proof) and drying with nitrogen. The wafer was then immersed into a colloidal solution containing negatively charged gold nanoparticles[44,45] (diameter, ~20 nm; concentration, 3.5×10^{11} particles/mL (5.8×10^{-10} M); Ted Pella Inc.) for 30 min at 4 °C. The pH of the gold colloid was 6.6 (measured with a pH meter; Oakton Acorn pH5) and did not change during or after sample immersion. After removal from the gold colloidal solution, the sample was immediately rinsed with methanol and dried with a stream of nitrogen. The samples were imaged with an FE-SEM (field-emission scanning electron microscope, ZEISS Supra 55 VP).

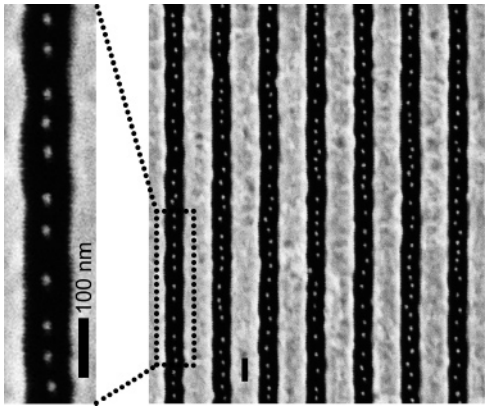

Figure 3. SEM image of Au nanoparticles (diameter ~20 nm) placed on silicon oxide lines using the electrostatic funneling scheme. In this SEM image, the gold lines appear bright and silicon oxide lines dark. Scale bars: 100 nm.

In Figure 3, we show a representative SEM image that demonstrates the effectiveness of the electrostatic funnel for a one-dimensional guidance structure. The SEM image shows that electrostatic guidance works extremely well and results in many Au nanoparticles simultaneously placed along the

centers of multiple silicon oxide lines. Although Figure 3 shows just one area, inspection of the 2 cm × 2 cm wafer piece showed that the nanoparticles were precisely placed over the entire piece. This procedure has been performed on many wafer pieces with the same result. The degree of precision for the guided nanoparticle placement shown in Figure 3 has been quantified by measuring the deviation of each nanoparticle from the centerline of the silicon oxide lines. From all 217 nanoparticles in Figure 3, including all outliers, the standard deviation is 6.2 nm. We also note that the nanoparticles are regularly spaced, with separation of ~50 nm, due to the repulsive forces between them. Their like charge combined with their close proximity in size, and thus in mass (<10% variation), creates a similar effective repelling distance for any pair of nanoparticles. (We find that this interparticle separation matches very well with theoretical calculations based on DLVO (Derjaguin, Landau, Verwey, and Overbeek) theory,[38,39,46] see the Supporting Information for details).

Electrostatic interactions between the particle and substrate surface are believed to be the dominant mechanism for the guided particle placement seen in Figure 3. First, we want to point out that the capillary forces, which have been successfully implemented for nanoparticle placement by other research groups,[27−29] are not likely to be responsible for the guided placement shown in Figure 3. Capillary force driven assembly requires the existence of an air−water interface at the surface patterns, but our experimental procedures do not produce this condition.[47]

The importance of electrostatic interaction is clearly seen in Figure 4, where we compare two wafers functionalized with SAMs of differing charge combinations. For one wafer (Figure 4A), silicon oxide and gold patterns were functionalized with positively and negatively charged molecules, using the SAMs described earlier (i.e., APTES and MHA, respectively). For the other wafer (Figure 4B), the same positively charged APTES SAMs were placed on the silicon oxide surface, but the negatively charged SAMs on the gold surface were replaced with nonpolar SAMs using *n*-octadecanethiol (ODT, $HS-(CH_2)_{17}-CH_3$, 98%; Sigma-Aldrich).[48] When the two samples were immersed into a colloid of Au nanoparticles (~20 nm diameter), the former set of SAMs created denuded zones with width of ~70 nm, Figure 4A. On the other hand, no denuded zone was found for the latter set of SAMs, Figure 4B. These images provide evidence of the importance of the magnitude of the electrostatic interaction energy gradient (in a direction parallel to the substrate) in guiding nanoparticles to the surface. Where the gradient is strong, the nanoparticles are funneled away from the boundary toward the center of the positively charged area, and where the gradient is weak, they are not.

The observations in Figures 3 and 4A clearly indicate that the interactions between Au nanoparticles and charged substrate are electrostatic and of long range, extending at least over tens of nanometers. To get a more quantitative picture of this long-range nanoparticle−substrate interaction, we have calculated the interaction energies based on DLVO theory.[38,39,46] We first calculate the interaction energy between

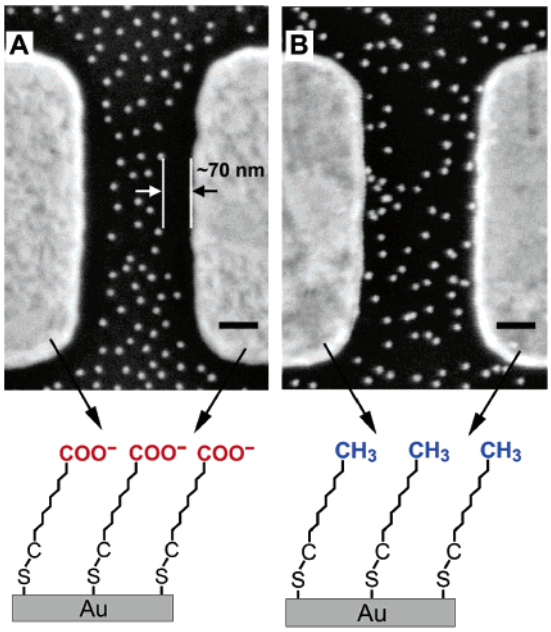

Figure 4. Control of guiding electrostatic interaction energy with different combinations of SAMs. (A) The gold surfaces (bright in the SEM image) were negatively charged with SAMs of MHA ($-COO^-$ terminated) while the silicon oxide surface (dark in the SEM image) was positively charged with SAMs of APTES ($-NH_3^+$ terminated). When immersed into the Au colloidal solution, Au nanoparticles (negatively charged, diameter ~20 nm) were guided away from gold surfaces and attracted onto silicon oxide surface, creating denuded zones with width of ~70 nm. (B) Under exactly the same conditions except that the gold surfaces were functionalized with nonpolar SAMs using ODT ($-CH_3$ terminated), we observe no denuded zone due to the absence of appreciable gradient of interaction energies in a direction parallel to the substrate. Scale bars: 100 nm.

a Au nanoparticle and an infinite surface functionalized with either MHA or APTES (geometry in parts A and B of Figure 5, respectively). The interaction energy $V_j(z)$ is a sum of electrical double-layer interaction energy $\Phi_j(z)$ and van der Waals interaction energy $W_j(z)$, where j represents the surface type (functionalized with either MHA or APTES)

$$V_{MHA}(z) = \Phi_{MHA}(z) + W_{MHA}(z)$$

and

$$V_{APTES}(z) = \Phi_{APTES}(z) + W_{APTES}(z) \quad (1)$$

The double-layer interaction energies, $\Phi_{MHA}(z)$ and $\Phi_{APTES}(z)$, can be calculated using linear superposition approximation[49−51] (LSA) and given by

$$\Phi_{MHA}(z) = 4\pi\epsilon\epsilon_0 a(kT/e)^2 Y_{Au} Y_{MHA} \exp(-\kappa z)$$

and

$$\Phi_{APTES}(z) = 4\pi\epsilon\epsilon_0 a(kT/e)^2 Y_{Au} Y_{APTES} \exp(-\kappa z) \quad (2)$$

where ϵ is the dielectric constant of water, ϵ_0 is the

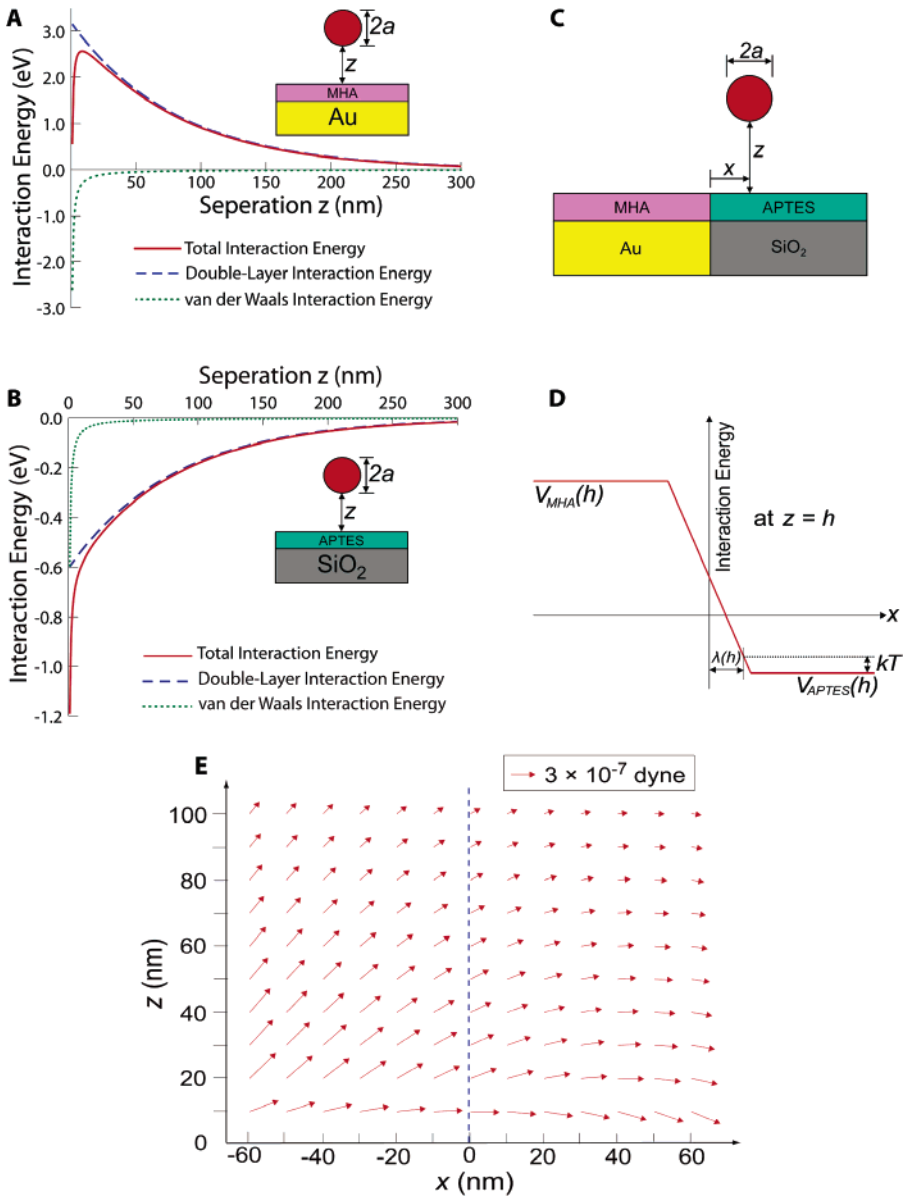

Figure 5. Calculation of the interaction energies. (A) Interaction energy between a 20 nm Au nanoparticle (a = 10 nm) and a MHA-functionalized substrate. (B) Interaction energy between a 20 nm Au nanoparticle (a = 10 nm) and an APTES-functionalized substrate. (C) A geometrical schematic for a nanoparticle interacting with a substrate functionalized with MHA for one side and APTES for the other side. (D) A schematic of the interaction energy as a function of x for a fixed z (=h) under the geometry in C. (E) Forces exerted on a 20 nm diameter Au nanoparticle under the geometry in C for $|x| < 70$ nm and $z \leq 100$ nm. The MHA−APTES boundary is located at x = 0 and indicated by the dotted line.

permittivity of free space, a is the radius of a Au nanoparticle, k is the Boltzmann constant, T is the absolute temperature, e is the unit charge of an electron, and Y_{Au}, Y_{MHA}, and Y_{APTES} are effective reduced surface potentials[49,52,53] of an *isolated* Au nanoparticle, an *isolated* MHA functionalized substrate, and an *isolated* APTES functionalized substrate, respectively. κ is the inverse Debye length defined by[38,46]

$$\kappa = [(1000e^2 N_A/\epsilon\epsilon_0 kT)\,\Sigma_i\, z_i^2 M_i]^{1/2} \qquad (3)$$

where N_A is Avogadro's number, z_i is the valency of ion species i and M_i is the molar ion concentration of ion species i. From eq 3, the Debye length κ^{-1} of our Au colloid[45] is calculated to be 81.5 nm.

Each of Y_{Au}, Y_{MHA}, and Y_{APTES} can be obtained by solving nonlinear Poisson−Boltzmann equations when ion concentrations M_i, valencies z_i, and surface charge densities σ_{Au}, σ_{MHA}, and σ_{APTES} are given. No exact analytical solution to the nonlinear Poisson−Boltzmann equations exists except for a planar geometry, but numerical solutions[52] as well as approximate analytic expressions[53,54] are available. Using the approximate analytic expressions by Ohshima,[53,54] along with known ion concentrations[45] and available surface charge densities σ_{Au}, σ_{MHA}, and σ_{APTES},[26,55,56] we obtain Y_{Au}, Y_{MHA}, and Y_{APTES} as −1.59, −5.62, and 1.07, respectively (see Supporting Information for calculation details). By inserting Y_{Au}, Y_{MHA}, and Y_{APTES} along with κ into eq 2, we obtain double-layer interaction energies $\Phi_{MHA}(z)$ and

$\Phi_{APTES}(z)$, which are plotted in parts A and B of Figure 5, respectively.

The van der Waals interaction energies $W_{MHA}(z)$ and $W_{APTES}(z)$ are given by[38]

$$W_{MHA}(z) = -A_{MHA}a/6z$$

and

$$W_{APTES}(z) = -A_{APTES}\,a/6z \qquad (4)$$

where A_{MHA} and A_{APTES} are the Hamaker constants for the system of Au/MHA/water/Au and SiO_2/APTES/water/Au,[57,58] the reported values of which are 2.5×10^{-19} and 5.7×10^{-20} J, respectively.[59,60] From eq 4, the van der Waals interaction energies $W_{MHA}(z)$ and $W_{APTES}(z)$ were obtained and are plotted in parts A and B of Figure 5, respectively.

From eqs 1−4, the total interaction energies $V_{MHA}(z)$ and $V_{APTES}(z)$ were obtained and are plotted in parts A and B of Figure 5. The calculation results shown in these plots reveal the nature of guiding forces seen in our experiments. The total interaction energies $V_{MHA}(z)$ and $V_{APTES}(z)$ are dominated by the electrostatic double-layer interactions as long as the nanoparticle−surface separation is more than 10 nm. For MHA functionalized substrates, the interaction with a Au nanoparticle is repulsive (positive interaction energies), and for APTES functionalized substrates, the interactions are attractive (negative interaction energies), as expected from the surface charge states of Au nanoparticles, MHA, and APTES. Most importantly, the plots clearly indicate that the interactions are indeed of long range: for the interaction of a Au nanoparticle with MHA functionalized substrates, the interaction energy $V_{MHA}(z)$ reaches the room temperature thermal energy (∼25 meV) at ∼370 nm away from the substrate (beyond the axis range in Figure 5A). For the interaction with APTES functionalized substrates, $V_{APTES}(z)$ reaches the thermal energy (ca. −25 meV) at ∼270 nm.

With the interaction energies $V_{MHA}(z)$ and $V_{APTES}(z)$ obtained, we now can get a more quantitative picture for the observed denuded zone in Figure 4A. When two surfaces functionalized with MHA and APTES are adjacent to each other (geometry in Figure 5C), we can semiquantitatively plot the interaction energy $V(x,z = h)$ between a Au nanoparticle and the substrate as follows. First, we note that when the nanoparticle is appreciably away from the MHA-APTES boundary (when $|x|$ is large), $V(x,z = h)$ assumes the value $V_{MHA}(h)$ or $V_{APTES}(h)$ because the influence of the other charged surface diminishes. Second, near the interface (when $|x|$ is small), $V(x,z = h)$ deviates from both $V_{MHA}(h)$ and $V_{APTES}(h)$ and assumes a value between them because the influence of negatively and positively charged surfaces overlaps. If we assume that variation of $V(x,z = h)$ is constant, i.e., $dV(x,z = h)/dx$ is constant, we obtain a plot for $V(x,z = h)$ as in Figure 5D. According to Figure 5D, the nanoparticle can approach the MHA−APTES boundary only up to $x = \lambda(h)$ because of the energy barrier. This effect produces the denuded zone observed in Figure 4A. We can further estimate the lateral force F_L $(=-\partial V(x,z)/\partial x|_{z=h})$ exerted on the Au nanoparticle. From geometrical consideration of Figure 5D, we get the relationship between $\partial V(x,z)/\partial x|_{z=h}$ and $\lambda(h)$ as

$$\partial V(x,z)/\partial x|_{z=h} = -\{(V_{MHA}(h) - V_{APTES}(h))/2 - kT\}/\lambda(h) \quad (5)$$

If we assume $\lambda(h)$ to be ∼70 nm (the width of the denuded zone in Figure 4A) when the Au nanoparticle comes close to the surface (say, $h \leq 100$ nm), eq 5 predicts the lateral force F_L $(=-\partial V(x,z)/\partial x|_{z=h})$ to be 3.6×10^{-7}, 3.2×10^{-7}, 2.9×10^{-7}, 2.5×10^{-7}, and 2.2×10^{-7} dyn for $h = 10$, 20, 30, 40, and 50 nm, respectively.[61] This lateral force F_L may be compared with the vertical force F_V $(=-V(x,z)/\partial z)$ and is found to be, at $x = 0$ for example, -9.4×10^{-9}, 1.4×10^{-7}, 1.5×10^{-7}, 1.4×10^{-7}, and 1.3×10^{-7} dyn for $h =$ 10, 20, 30, 40, and 50 nm, respectively. Figure 5E summarizes the forces exerted on a 20 nm diameter Au nanoparticle obtained from eq 5 and Figure 5D through

$$\vec{F}(x,z) = -\frac{\partial V(x,z)}{\partial x}\vec{x} - \frac{\partial V(x,z)}{\partial z}\vec{z} \qquad (6)$$

where $\vec{x}$ and $\vec{z}$ are unit vectors along x and z directions. Although our calculations are semiquantitative, the results present clear indication that the lateral forces become comparable to or greater than the vertical forces near the MHA−APTES boundary ($|x| < 70$ nm). These strong lateral forces are responsible for the guided nanoparticle placement as observed in Figure 3 and Figure 4A.

The long-range electrostatic interactions and strong lateral forces can allow the guided nanoparticle placement for various geometries. What is required is the creation of an appropriate electrostatic funnel on the substrate. For example, a simple change in the surface pattern from line to dot can create a guiding potential sufficient to place individual nanoparticles onto targeted places. This is demonstrated in Figure 6 with an array of square-shaped patterns and ∼20

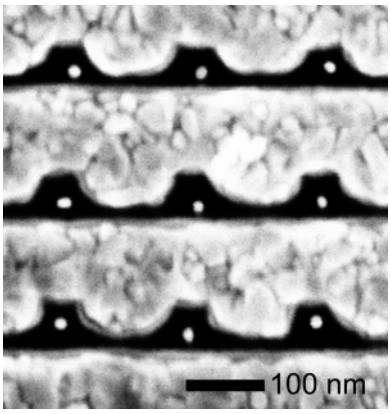

Figure 6. Zero-dimensional placement of individual nanoparticles (∼20 nm diameter): the patterns in dark, silicon oxide functionalized with APTES SAMs; the bright area, gold surface functionalized with MHA SAMs. The Au nanoparticles appear as bright dots. Note that only one nanoparticle is placed in the center of each square-shaped pattern due to the repulsive electrostatic interactions between charged nanoparticles (see the Supporting Information).

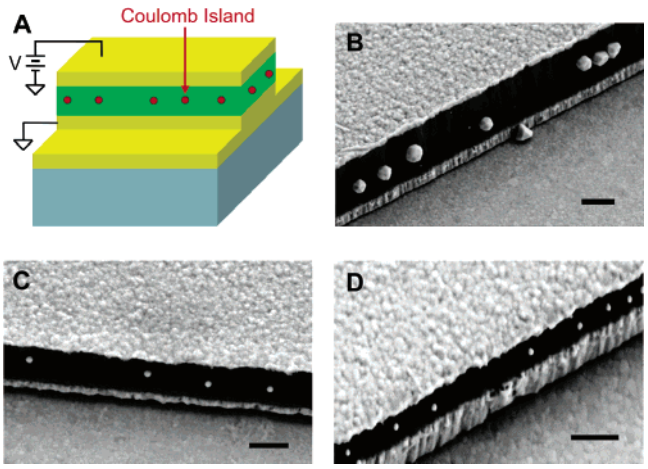

Figure 7. Nanoparticle placement in a step structure. (A) A new device architecture in which two electrodes are positioned vertically and nanoparticles are precisely placed in the center of the electrode gap. (B−D) SEM images for the architecture in (A) demonstrating the effectiveness of guided placement. The diameter of Au nanoparticles is ∼200, ∼80, and ∼50 nm for (B), (C), and (D), respectively. Scale bars: 400 nm.

nm Au nanoparticles. (It is also worth noting that only one nanoparticle is positioned in each square due to repulsive forces between negatively charged Au nanoparticles: once one nanoparticle occupies one pattern, it prohibits the approach of other nanoparticles.) In addition, the creation of the guiding potential is not constrained to rely on the surface pattern but can utilize the exposed sidewall surface of thin film layers as shown in Figure 7A. Parts B−D of Figure 7 demonstrate the successful fabrication of such a structure: Au nanoparticles of diameter ∼200, ∼80, and ∼50 nm placed on silicon oxide sidewalls (positively charged with APTES) sandwiched between two gold electrodes (negatively charged with MHA).[62] The effectiveness of guided placement is clearly maintained in these step structures as the nanoparticles are observed only on the *center* locations of the oxide stripes (the exposed sidewalls).

We expect that the electrostatic funneling method demonstrated here using nanoparticles can also be used for the controlled placement of other nanoscale building blocks. For example, controlled placement of one-dimensional systems such as nanowires or carbon nanotubes could be realized using one-dimensional guiding structures similar to the one demonstrated in Figure 3. Furthermore, extension of the proven ability to construct the device architecture in Figure 7A could lead to wafer-scale fabrication of room-temperature single electron devices when ∼5 nm nanoparticles are used and the electrode gap (i.e., the *thickness* of the silicon oxide sidewall) is reduced to ∼10 nm.[63,64] Currently available thin film deposition/growth techniques such as ALD (atomic layer deposition) or PECVD (plasma enhanced chemical vapor deposition) are capable of producing the required layer thickness with subnanometer precision.[65]

We have demonstrated the ability of the electrostatic funnel guiding method to place nanoparticles with nanometer scale precision on much coarser guidance structures defined using conventional CMOS technology. The practicality of electrostatic funneling, that is, its simplicity and compatibility with CMOS fabrication and packaging technology, combined with the fact that the method works for both lateral and vertical patterns, may provide a viable pathway to the wafer-scale[66] fabrication of integrated systems of nanoscale devices and sensors.

Acknowledgment. We thank Dr. Nancy Michael for valuable discussions. This work was supported by the Office of Naval Research (N00014-05-1-0030), National Science Foundation CAREER grant (ECS-0449958), and Advanced Research Program of Texas Higher Education Coordinating Board (003656-0014−2006).

Supporting Information Available: Calculation details for the interaction energies between two Au nanoparticles and the effective reduced surface potentials Y_{Au}, Y_{MHA}, and Y_{APTES}. This material is available free of charge via the Internet at http://pubs.acs.org.

References

(1) Klein, D. L.; Roth, R.; Lim, A. K. L.; Alivisatos, A. P.; McEuen, P. L. *Nature* **1997**, *389*, 699−701.
(2) Alivisatos, P. *Nat. Biotechnol.* **2004**, *22*, 47−52.
(3) Fan, H. Y.; Yang, K.; Boye, D. M.; Sigmon, T.; Malloy, K. J.; Xu, H. F.; Lopez, G. P.; Brinker, C. J. *Science* **2004**, *304*, 567−571.
(4) Huang, Y.; Duan, X.; Cui, Y.; Lauhon, L. J.; Kim, K.-H.; Lieber, C. M. *Science* **2001**, *294*, 1313−1317.
(5) Wang, J.; Gudiksen, M. S.; Duan, X.; Cui, Y.; Lieber, C. M. *Science* **2001**, *293*, 1455−1457.
(6) Duan, X.; Huang, Y.; Cui, Y.; Wang, J.; Lieber, C. M. *Nature* **2001**, *409*, 66−69.
(7) Duan, X.; Huang, Y.; Agarwal, R.; Lieber, C. M. *Nature* **2003**, *421*, 241−245.
(8) Cui, Y.; Lieber, C. M. *Science* **2001**, *291*, 851−853.
(9) Favier, F.; Walter, E. C.; Zach, M. P.; Benter, T.; Penner, R. M. *Science* **2001**, *293*, 2227−2231.
(10) Chen, J.; Perebeinos, V.; Freitag, M.; Tsang, J.; Fu, Q.; Liu, J.; Avouris, P. *Science* **2005**, *310*, 1171−1174.
(11) Heinze, S.; Tersoff, J.; Martel, R.; Derycke, V.; Appenzeller, J.; Avouris, P. *Phys. Rev. Lett.* **2002**, *89*, 106801.
(12) Tans, S. J.; Verschueren, A. R. M.; Dekker, C. *Nature* **1998**, *393*, 49−52.
(13) Nicewarner-Pena, S. R.; Freeman, R. G.; Reiss, B. D.; He, L.; Pena, D. J.; Walton, I. D.; Cromer, R.; Keating, C. D.; Natan, M. J. *Science* **2001**, *294*, 137−141.
(14) Park, S.-J.; Taton, T. A.; Mirkin, C. A. *Science* **2002**, *295*, 1503−1506.
(15) Cui, Y.; Wei, Q.; Park, H.; Lieber, C. M. *Science* **2001**, *293*, 1289−1292.
(16) Chan, W. C. W.; Nie, S. M. *Science* **1998**, *281*, 2016−2018.
(17) Huang, Y.; Duan, X.; Wei, Q.; Lieber, C. M. *Science* **2001**, *291*, 630−633.
(18) Tsukruk, V. V.; Ko, H.; Peleshanko, S. *Phys. Rev. Lett.* **2004**, *92*, 065502.
(19) Smith, P. A.; Nordquist, C. D.; Jackson, T. N.; Mayer, T. S.; Martin, B. R.; Mbindyo, J.; Mallouk, T. E. *Appl. Phys. Lett.* **2000**, *77*, 1399−1401.
(20) Zhang, Y.; Chang, A.; Cao, J.; Wang, Q.; Kim, W.; Li, Y.; Morris, N.; Yenilmez, E.; Kong, J.; Dai, H. *Appl. Phys. Lett.* **2001**, *79*, 3155−3157.
(21) Tanase, M.; Bauer, L. A.; Hultgren, A.; Silevitch, D. M.; Sun, L.; Reich, D. H.; Searson, P. C.; Meyer, G. J. *Nano Lett.* **2001**, *1*, 155−158.
(22) Wang, Y. H.; Maspoch, D.; Zou, S. L.; Schatz, G. C.; Smalley, R. E.; Mirkin, C. A. *Proc. Natl. Acad. Sci. U.S.A.* **2006**, *103*, 2026−2031.
(23) Rao, S. G.; Huang, L.; Setyawan, W.; Hong, S. H. *Nature* **2003**, *425*, 36−37.
(24) Hannon, J. B.; Afzali, A.; Klinke, C.; Avouris, P. *Langmuir* **2005**, *21*, 8569−8571.

(25) Myung, S.; Im, J.; Huang, L.; Rao, S. G.; Kim, T.; Lee, D. J.; Hong, S. H. *J. Phys. Chem. B* **2006**, *110*, 10217−10219.
(26) Kumagai, S.; Yoshii, S.; Yamada, K.; Matsukawa, N.; Fujiwara, I.; Iwahori, K.; Yamashita, I. *Appl. Phys. Lett.* **2006**, *88*, 153103.
(27) Cui, Y.; Bjork, M. T.; Liddle, J. A.; Sonnichsen, C.; Boussert, B.; Alivisatos, A. P. *Nano Lett.* **2004**, *4*, 1093−1098.
(28) Xia, Y. N.; Yin, Y. D.; Lu, Y.; McLellan, J. *Adv. Funct. Mater.* **2003**, *13*, 907−918.
(29) Gordon, M. J.; Peyrade, D. *Appl. Phys. Lett.* **2006**, *89*, 053112.
(30) Zheng, J. W.; Constantinou, P. E.; Micheel, C.; Alivisatos, A. P.; Kiehl, R. A.; Seeman, N. C. *Nano Lett.* **2006**, *6*, 1502−1504.
(31) Warner, M. G.; Hutchison, J. E. *Nat. Mater.* **2003**, *2*, 272−277.
(32) Braun, E.; Eichen, Y.; Sivan, U.; Ben-Yoseph, G. *Nature* **1998**, *391*, 775−778.
(33) Fu, X. Y.; Wang, Y.; Huang, L. X.; Sha, Y. L.; Gui, L. L.; Lai, L. H.; Tang, Y. Q. *Adv. Mater.* **2003**, *15*, 902−906.
(34) Dujardin, E.; Peet, C.; Stubbs, G.; Culver, J. N.; Mann, S. *Nano Lett.* **2003**, *3*, 413−417.
(35) Nakao, H.; Shiigi, H.; Yamamoto, Y.; Tokonami, S.; Nagaoka, T.; Sugiyama, S.; Ohtani, T. *Nano Lett.* **2003**, *3*, 1391−1394.
(36) Demers, L. M.; Ginger, D. S.; Park, S. J.; Li, Z.; Chung, S. W.; Mirkin, C. A. *Science* **2002**, *296*, 1836−1838.
(37) The electrical double layer is formed due to rearrangement (screening) of ions that are present in the liquid medium. Its electrostatic potentials and charge densities are described by the Poisson−Boltzmann equation. When the nanoparticles come very close to the substrate, the van der Waals interaction also contributes to the interaction energy. More details can be found in the later part of this paper. See also refs 38−39.
(38) Israelachvili, J. *Intermolecular and Surface Forces*, 2nd ed.; Academic Press: London; San Diego, 1991.
(39) Verwey, E. J. W.; Overbeek, J. T. G. *Theory of the Stability of Lyophobic Colloids*; Elsevier: Amsterdam, 1948.
(40) Wolf, S. *Silicon Processing for the VLSI Era, Vol. 4: Deep-Submicron Process Technology*; Lattice Press: Sunset Beach, 2002.
(41) Plating solution from Alfa Aesar (major components: $KAu(CN)_2$, NH_4OH, and water). Electroless plating condition: 65 °C for 45 s.
(42) Onclin, S.; Ravoo, B. J.; Reinhoudt, D. N. *Angew. Chem., Int. Ed.* **2005**, *44*, 6282−6304.
(43) Smith, R. K.; Lewis, P. A.; Weiss, P. S. *Prog. Surf. Sci.* **2004**, *75*, 1−68.
(44) The citrate ions in the gold colloid are strongly adsorbed on the gold nanoparticle surface and are deprotonated at the pH level of our experiment, resulting in negatively charged nanoparticles. See also ref 55.
(45) The aqueous gold colloidal solution contains Na^+, citrate ions ($C_6O_7H_7^-$, $C_6O_7H_6^{2-}$, $C_6O_7H_5^{3-}$), Cl^-, H_3O^+, and OH^- (see, for example, ref 55). Their concentrations are (from the measured pH of 6.6, known dissociation constants of citrate ions, and private communication with Ted Pella Inc.): $[Na^+] = 7.8 \times 10^{-6}$ M, $[C_6O_7H_7^-] = 1.5 \times 10^{-8}$ M, $[C_6O_7H_6^{2-}] = 1.0 \times 10^{-6}$ M, $[C_6O_7H_5^{3-}] = 1.6 \times 10^{-6}$ M, $[Cl^-] = 1.2 \times 10^{-6}$ M, $[H_3O^+] = 2.5 \times 10^{-7}$ M, $[OH^-] = 4.0 \times 10^{-8}$ M.
(46) Hiemenz, P. C. *Principles of Colloid and Surface Chemistry*; Marcel Dekker: New York, 1977.
(47) First, both MHA and APTES functionalized surfaces are hydrophilic, so that when the sample is removed from the aqueous solution of gold colloid, the sample is completely covered with a film of water and produces no water−air interface near the surface patterns. Second, while the sample is entirely covered with the water film, it is immediately immersed into a large volume of pure methanol to rinse unattached nanoparticles from the substrate. When the sample is finally removed from the methanol for drying with nitrogen, no unattached nanoparticles are present to contribute to capillary force driven assembly. Also, if the capillary force were instrumental in the observed nanoparticle placement, the amount of immersion time in the Au colloidal solution would be irrelevant. However, if the immersion time is reduced to a few minutes ($<\sim$4 min), with everything else kept exactly the same, we find almost no attachment of Au nanoparticles on the substrate. This serves as another direct evidence that capillary forces are not responsible for the observed nanoparticle placement.
(48) The SAMs of ODT were formed by immersing into 5 mM ODT solution in hexadecane for 42 h at 40 °C, followed by rinsing with warm (40 °C) acetone and drying with nitrogen.
(49) Bell, G. M.; Levine, S.; McCartney, L. N. *J. Colloid Interface Sci.* **1970**, *33*, 335−359.
(50) Warszynski, P.; Adamczyk, Z. *J. Colloid Interface Sci.* **1997**, *187*, 283−295.
(51) Adamczyk, Z.; Warszynski, P. *Adv. Colloid Interface Sci.* **1996**, *63*, 41−149.
(52) Loeb, A. L.; Overbeek, J. T. G.; Wiersema, P. H. *The Electrical Double Layer Around a Spherical Colloid Particle*; MIT Press: Cambridge, 1960.
(53) Ohshima, H. *J. Colloid Interface Sci.* **1995**, *174*, 45−52.
(54) Ohshima, H. *J. Colloid Interface Sci.* **1995**, *171*, 525−527.
(55) Biggs, S.; Mulvaney, P.; Zukoski, C. F.; Grieser, F. *J. Am. Chem. Soc.* **1994**, *116*, 9150−9157.
(56) Kane, V.; Mulvaney, P. *Langmuir* **1998**, *14*, 3303−3311.
(57) The value of the Hamaker constant is dominated by substrate materials and medium, and the effect of SAMs on Hamaker constant is negligible as long as the separation is larger than ∼5 nm. See, for example, ref 58.
(58) Israelachvili, J. N.; Tabor, D. *Proc. R. Soc. London, Ser. A* **1972**, *331*, 19−38.
(59) Biggs, S.; Mulvaney, P. *J. Chem. Phys.* **1994**, *100*, 8501−8505.
(60) Barten, D.; Kleijn, J. M.; Duval, J.; von Leeuwen, H. P.; Lyklema, J.; Stuart, M. A. C. *Langmuir* **2003**, *19*, 1133−1139.
(61) Because $\lambda(h)$ decreases as h increases, this value is a low-bound estimate.
(62) The concentrations of Au nanoparticles were 7.0×10^8, 5.5×10^9, and 2.3×10^{10} (particles/mL), the immersion times were 30, 20, and 10 min, and the immersion temperatures were room temperature, 4 °C, and 4 °C for 200, 80, and 50 nm Au nanoparticles, for parts B, C, and D of Figure 7, respectively. All Au nanoparticles from Ted Pella Inc.
(63) Likharev, K. K. *Proc. IEEE* **1999**, *87*, 606−632.
(64) Grabert, H.; Devoret, M. H., Eds. *Single Charge Tunneling*; Plenum: New York, 1992.
(65) Note, on the other hand, that with current *lateral* pattern definition techniques such as photolithography, it is difficult to define patterns with resolution better than a few tens of nanometers. Other techniques such as e-beam writing and scanning probe microscopy are too slow for large-scale applications.
(66) Here, "wafer-scale" refers to the simultaneous fabrication of millions of devices on a single wafer.

NL062727C